

LLT: Local Linear Transformer for PDE Operator Learning

Oded Ovadia*¹ and Eli Turkel^{†1}

¹School of Mathematical Sciences, Tel Aviv University, Tel Aviv, Israel

Abstract

Neural operators have become a common approach for learning PDE solution maps and accelerating numerical simulations. Transformer-based neural operators are of particular interest, since attention can learn long-range dependencies in the computational domain. However, standard attention has two major limitations when applied to PDEs: it scales quadratically with the number of computational nodes, and it lacks an explicit bias toward local interactions. To address these issues, we introduce Local Linear Transformer (LLT) for PDE operator learning. The architecture combines linear global attention with local spatial mixing, and incorporates coordinate and geometry information. We evaluate LLT on several PDE problems, including elasticity, plasticity, airfoil flow, pipe flow, and Darcy flow. The reference data for these problems span finite-element, finite-volume, and finite-difference discretizations on structured and unstructured meshes. Compared with other neural-operator and transformer baselines from prior studies, LLT achieves competitive or lower relative L_2 error across these problems. On matched structured discretizations, wall-clock time per training iteration is reduced by factors of 1.8 to 2.5 relative to Transolver. We also scale the approach and apply it to a three-dimensional car aerodynamics dataset with 32,186 unstructured mesh points per sample. Together, these results indicate that LLT provides an accurate and computationally efficient operator for PDE problems across discretizations, mesh types, and problem settings.

Keywords: partial differential equations, neural operators, transformers, scientific machine learning

1 Introduction

The use of machine learning (ML) methods for scientific computing has been growing rapidly in recent years, with many successful methods for modeling mathematical problems [Raissi, Perdikaris, and Karniadakis, 2019, Lu, Jin, Pang, Zhang, and Karniadakis, 2021, Li, Kovachki, Azizzadenesheli, Liu, Bhattacharya, Stuart, and Anandkumar, 2021, Long, Lu, Ma, and Dong, 2018, Xu, Chang, and Zhang, 2019, Takamoto, Praditia, Leiteritz, MacKinlay, Alesiani, Pflüger, and Niepert, 2022, Gupta and Brandstetter, 2022]. Such methods have shown promise in many different areas, including computational mechanics [Cai, Mao, Wang, Yin, and Karniadakis, 2021, Zhang, Kahana, Turkel, Ranade, Pathak, and Karniadakis, 2022], wave propagation [Ovadia, Kahana, Turkel, and Dekel, 2021, Ovadia, Kahana, and Turkel, 2024b], materials science [Dingreville, Stewart, and Chen, 2020, Oommen, Shukla, Goswami, Dingreville, and Karniadakis, 2022], fluid dynamics [Sharma, Chung, Akoush, and Ihme, 2023, Zhao, Zhang, Lou, Wang, and Yang, 2024], and turbulent flows [Wu, Xiao, and Paterson, 2018, Wang, Kashinath, Mustafa, Albert, and Yu, 2020].

*Corresponding author. Email: odedovadia@mail.tau.ac.il

[†]Email: turkel@tauex.tau.ac.il

In many applications, the same class of PDEs must be solved repeatedly for varying coefficients, geometries, initial conditions, or boundary conditions. Classical solvers remain the reference method for accuracy, but they can be expensive when thousands of related solves are required. This has motivated neural operators that learn solution maps directly from data. Neural operators provide one such framework by learning maps between input functions and output solution fields [Kovachki, Li, Liu, Azizzadenesheli, Bhattacharya, Stuart, and Anandkumar, 2023, Azizzadenesheli, Kovachki, Li, Liu-Schiaffini, Kossafi, and Anandkumar, 2024].

In particular, the Transformer architecture is a promising candidate for operator learning because its attention mechanism can learn information between distant points in the computational domain [Vaswani, Shazeer, Parmar, Uszkoreit, Jones, Gomez, Kaiser, and Polosukhin, 2017, Li, Meidani, and Farimani, 2023a, Hao, Wang, Su, Ying, Dong, Liu, Cheng, Song, and Zhu, 2023]. In PDE problems, boundary conditions, material interfaces, and elliptic coupling can introduce nonlocal dependence across the domain [Kovachki et al., 2023, Azizzadenesheli et al., 2024]. However, Transformers also face important difficulties in this setting. First, self-attention scales as $\mathcal{O}(N^2)$ in the number of spatial points, which becomes costly on high-resolution grids [Vaswani et al., 2017, Katharopoulos, Vyas, Pappas, and Fleuret, 2020, Choromanski, Likhoshesterov, Dohan, Song, Gane, Sarlos, Hawkins, Davis, Mohiuddin, Kaiser, Belanger, Colwell, and Weller, 2021, Wu, Luo, Wang, Wang, and Long, 2024]. Second, standard attention has no built-in bias toward local interactions. Many PDE solutions contain strong local structure, and classical numerical methods often exploit this structure through stencils or elements [Hughes, 2012, Godunov and Bohachevsky, 1959, Eymard, Gallouët, and Herbin, 2000]. This locality is especially important for hyperbolic PDEs, where information propagates along characteristics and the solution over a short time interval depends only on a limited region of the domain [LeVeque, 2002]. A purely global attention mechanism can therefore spend computation on interactions that are weak or irrelevant for the local update.

These requirements lead to a specific architectural design. A Transformer-based operator should communicate across the sampled domain while also emphasizing the local structure present in solution fields. It must also scale well with the number of nodes in order to operate on realistic grids. Finally, it should apply to both structured meshes and unstructured node sets, since reference data in operator-learning benchmarks may come from finite-element, finite-volume, and finite-difference discretizations. This motivates a model that combines efficient domain-wide communication with an explicit local mixing path, using linear attention to keep the attention cost close to linear in the number of points [Katharopoulos et al., 2020, Choromanski et al., 2021].

We propose LLT (**L**ocal **L**inear **T**ransformer) for supervised PDE operator learning. The model takes input fields sampled on a finite set of points and predicts the corresponding output fields at the same points. It uses kernelized linear attention for global communication and a local mixing path for spatial neighborhoods. It also includes coordinate encodings, a distance-to-reference-grid encoding, and a skip-connected decoder. Together, these components address the two main Transformer limitations described above by reducing the cost of attention and adding an explicit bias toward local interactions.

We evaluate LLT on five widely used PDE problems covering elasticity, plasticity, airfoil, pipe flow, and Darcy flow [Li, Huang, Liu, and Anandkumar, 2023c, Wu et al., 2024, Luo, Wu, Zhou, Xing, Di, Wang, and Long, 2025]. Reference data for these problems were generated with finite-element, finite-volume, and finite-difference solvers (Section 4). We also apply the model to a three-dimensional car aerodynamics dataset to test scaling to large unstructured meshes. The computational study provides the relative L_2 error across the five benchmark problems, along with a separate matched timing and memory comparison on structured discretizations. These results are used to assess both the accuracy of and the computational cost of the local-global attention design. We find that LLT achieves accurate results on these problems in comparison to other leading neural operator methods. The computational cost analysis further shows that

on matched structured grids of the same size, LLT scales well and is able to remain relatively fast and efficient.

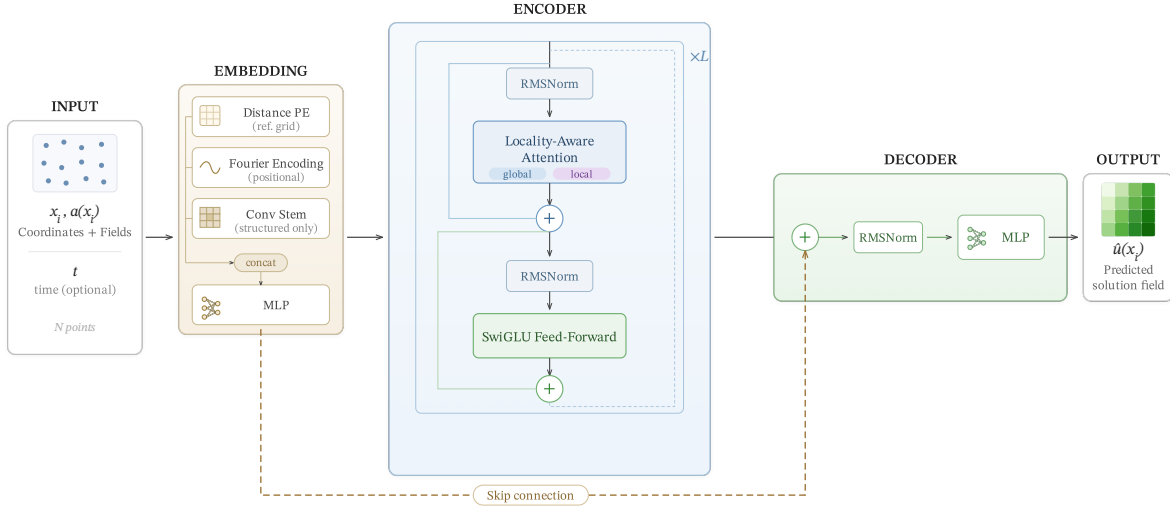


Figure 1: Architecture of LLT. Input coordinates and field values at N points are encoded in parallel through distance-based, Fourier, and convolutional branch channels, concatenated, and projected by a multilayer perceptron (MLP) into a fixed-width feature vector per point. A stack of L Transformer encoder blocks then refines this representation; each layer normalizes its input (RMSNorm), applies a global information-exchange step across all points together with a local spatial mixing step, and adds the result back to the input through a residual path, followed by a second normalization and a pointwise nonlinear transformation (SwiGLU). The decoder merges the processed output with a direct connection from the initial embedding and maps the result through a final MLP to produce the predicted solution field.

2 Related Work

Neural operators Neural operators learn mappings between function spaces, such as solution operators of partial differential equations [Azizzadenesheli et al., 2024]. Given an input function such as coefficients, source terms, or boundary and initial conditions, a neural operator predicts the corresponding solution field [Kovachki et al., 2023]. DeepONet is an early example of this approach, using a branch-trunk architecture to encode input functions and spatial query locations [Lu et al., 2021].

Another class of neural operators is based on spectral representations. Fourier Neural Operators (FNOs) use spectral convolutions for efficient global mixing on regular grids and are a standard baseline for PDE modeling [Li et al., 2021]. Related works have extended operator learning to more complex discretizations and geometries, including graph-based constructions for irregular meshes [Li, Kovachki, Azizzadenesheli, Liu, Bhattacharya, Stuart, and Anandkumar, 2020] and deformation-based approaches that map general domains to latent regular grids before applying spectral operators [Li et al., 2023c]. Hybrid formulations can also add physical structure, for example, by enforcing PDE residuals during training [Li, Zheng, Kovachki, Jin, Chen, Liu, Azizzadenesheli, and Anandkumar, 2024].

Transformers for PDEs. Transformers model long-range interactions through attention and handle irregular sampling more directly than architectures tied to a fixed grid [Vaswani et al., 2017, Hao et al., 2023]. For example, OFormer formulates operator learning using self-

and cross-attention between observed input samples and query points, reducing reliance on grid-specific inductive biases while achieving strong performance on standard PDE test problems [Li et al., 2023a]. Subsequent work developed attention variants for multi-scale structure and heterogeneous discretizations [Hao et al., 2023].

Other works focus on hybrid methods, combining Transformers with other components. For example, ViTO pairs a U-Net encoder with vision Transformer blocks to capture local and global structures [Ovadia, Kahana, Stinis, Turkel, Givoli, and Karniadakis, 2024a, Taccari, Ovadia, Wang, Chen, Kahana, and Jimack, 2023]. TC-UNet extends this design to time-dependent operators by conditioning a U-Net backbone on time with Transformer attention, enabling continuous-in-time inference without temporal discretization at test time [Ovadia, Oommen, Kahana, Peyvan, Turkel, and Karniadakis, 2025]. Another approach is to combine neural operators with classical numerical methods to achieve convergence at both large and small scales [Zhang, Kahana, Kopaničáková, Turkel, Ranade, Pathak, and Karniadakis, 2024, Ovadia et al., 2024b]. Other works focus on integrating physics-informed aspects into the Transformer architecture and training procedure [Zhao, Ding, and Prakash, 2023, Lorsung, Li, and Barati Farimani, 2024].

A key challenge in Transformer-based PDE models is the quadratic cost of global attention [Vaswani et al., 2017, Katharopoulos et al., 2020, Choromanski et al., 2021, Wu et al., 2024]. This is especially troublesome at high spatial resolutions, so recent methods emphasize scalable attention mechanisms and structured tokenization [Li, Shu, and Farimani, 2023b, Wu et al., 2024, Luo et al., 2025]. Transolver introduces Physics-Attention, which groups mesh points into learnable slices and performs attention at the slice level, yielding linear computational complexity while retaining accuracy on complex geometries [Wu et al., 2024]. Transolver++ extends this approach to larger inputs by improving parallelism and using a more efficient attention [Luo et al., 2025].

Linear attention. Linear attention methods reduce the cost of attention by replacing the softmax kernel with feature maps, allowing key-value aggregation to be computed once and reused for every query. This idea appears in Linear Transformers and related kernelized attention methods [Katharopoulos et al., 2020, Choromanski et al., 2021]. Several works have successfully applied linear attention to PDE modeling [Hao et al., 2023, Tran, Mathews, Xie, and Ong, 2021]. At the same time, other studies have shown that some forms of linear attention can degrade performance and prevent the model from learning useful interactions [Wu, Wu, Xu, Wang, and Long, 2022].

Spatial and geometric encodings. Coordinate encodings are commonly used when neural networks represent spatial fields. Fourier feature mappings can help multilayer perceptrons represent high-frequency variation in coordinates [Mildenhall, Srinivasan, Tancik, Barron, Ramamoorthi, and Ng, 2020, Tancik, Srinivasan, Mildenhall, Fridovich-Keil, Raghavan, Singhal, Ramamoorthi, Barron, and Ng, 2020], and related periodic representations have been used to model spatial signals and their derivatives [Sitzmann, Martel, Bergman, Lindell, and Wetzstein, 2020]. In operator learning, coordinate information is also important because the input and output fields are sampled at physical locations rather than at abstract token indices. Several neural-operator architectures therefore include coordinate or geometry information to support prediction across resolutions, meshes, and domains [Li et al., 2021, 2023c, Li, Kovachki, Choy, Li, Kossaifi, Otta, Nabian, Stadler, Hundt, Azizzadenesheli, et al., 2023d, Li et al., 2023a].

Taken together, these lines of work highlight a central challenge for PDE operator learning: how to exchange information efficiently across the domain while incorporating relevant spatial structure. LLT studies a direct approach to this challenge by combining linear kernelized attention for global exchange with an explicit local branch for neighborhood structure.

3 Methodology

This section describes the LLT architecture. We first give a concise overview of the core design: how the model acts on a finite point set, what information each point carries, and how global and local mixing are combined. The subsections below then develop the operator-learning setup, the geometry-aware embedding, the encoder, and the decoder in full.

We study supervised learning of PDE solution operators on that discretization. The model observes input field samples at each location and predicts the corresponding solution samples at the same points. This pointwise view covers structured meshes, where nodes carry an implicit grid topology, and unstructured node sets with no fixed (i, j) layout.

LLT implements the learned operator as a Transformer over these point features (referred to as *tokens* in the Transformer literature). Each location is represented by its coordinates, any input field values available at that point, and geometry encodings that help distinguish position within the domain. A depth- L encoder updates all point features through residual blocks that pair kernelized linear attention, for near-linear-cost exchange across the full discretization, with a separate local mixing path for spatial neighborhoods. A lightweight decoder maps the final features to the predicted solution field. Structured and unstructured cases share this pointwise formulation, the global attention path, and the decoder; they differ only in how local neighborhoods are built (convolutional mixing on grids versus masked attention on a fixed-radius neighbor graph), as used in the experiments of Section 4.

3.1 Problem Setup

Let $\Omega \subset \mathbb{R}^{d_x}$ be the spatial domain. The input field is $a : \Omega \rightarrow \mathbb{R}^{d_a}$ and the solution field is $u : \Omega \rightarrow \mathbb{R}^{d_u}$. Given a discretization $\{x_i\}_{i=1}^N$, the model observes samples of a and predicts samples of u at the same points. The learned operator is

$$\mathcal{G}_\theta : a \mapsto u, \tag{1}$$

implemented as a neural network over the sampled point set.

3.2 Geometry-aware Embedding

For each point x_i , the embedder forms a feature vector from the coordinates and the input field value $a(x_i)$ when present. We augment these with two geometry encodings constructed from the coordinates.

The first is a distance encoding relative to a fixed reference set $\{\tilde{x}_m\}_{m=1}^R$. It records the point’s position relative to this reference:

$$d(x_i) = \left[\|x_i - \tilde{x}_m\|_2 \right]_{m=1}^R. \tag{2}$$

The second is a Fourier coordinate embedding that captures high-frequency spatial variation [Mildenhall et al., 2020, Tancik et al., 2020]:

$$\gamma(x_i) = \text{Concat}(\{\sin(2^b x_i^{(d)}), \cos(2^b x_i^{(d)})\}_{d=1}^{d_x} \}_{b=0}^{B-1}), \tag{3}$$

with fixed frequency bands $\{2^b\}_{b=0}^{B-1}$. The raw pointwise input is then

$$s_i = \text{Concat}(\gamma(x_i), x_i, d(x_i), a(x_i)), \tag{4}$$

and a small multilayer perceptron maps it to the encoder width:

$$e_i = \text{MLP}_{\text{emb}}(s_i) \in \mathbb{R}^D. \tag{5}$$

For structured discretizations, the distance encoding can be precomputed; for unstructured node sets, it is computed from the sample coordinates. Structured cases can also use a convolutional branch composed of a short stack of convolution layers applied to the concatenated coordinates and field values. That replaces the separate x_i and $a(x_i)$ terms in s_i with a learned local feature, giving the model a local spatial bias from the first layer. This encoding operates as a learned geometric input that helps the network distinguish points with similar coordinates but different positions relative to the sampled domain.

3.3 Encoder

The encoder uses pre-normalized residual blocks. Each block applies an LLT mixing layer followed by a pointwise nonlinear transformation:

$$\begin{aligned}\hat{\mathbf{H}}^\ell &= \text{Attention}(\text{RMSNorm}(\mathbf{H}^{\ell-1})) + \mathbf{H}^{\ell-1}, \\ \mathbf{H}^\ell &= \text{FFN}(\text{RMSNorm}(\hat{\mathbf{H}}^\ell)) + \hat{\mathbf{H}}^\ell,\end{aligned}\tag{6}$$

where $\mathbf{H}^\ell \in \mathbb{R}^{N \times D}$ holds the pointwise features at layer ℓ . The Attention operator is a weighted combination of a global linear-attention path and a local spatial-mixing path; its full form is given in Eq. (14). The remaining components of the residual block are defined next. The normalization

$$\text{RMSNorm}(x)_c = \frac{x_c}{\sqrt{\frac{1}{D} \sum_{c'=1}^D x_{c'}^2 + \epsilon}}\tag{7}$$

rescales each feature vector by its root-mean-square magnitude [Zhang and Sennrich, 2019]. The feedforward network uses a gated form [Shazeer, 2020] in which the SiLU activation $\text{silu}(x) = x \sigma(x)$, where σ is the logistic sigmoid, gates a parallel linear projection:

$$\text{FFN}(h) = W_o \left(\text{silu}(W_g h) \odot (W_u h) \right),\tag{8}$$

where \odot denotes the elementwise (Hadamard) product. This gated feedforward provides a stronger pointwise nonlinearity than a single linear layer followed by one activation.

The mixing layer has two paths. The global path uses kernelized linear attention with n_h parallel heads. For each head, the input features are projected to queries, keys, and values through learned matrices:

$$\mathbf{Q} = \mathbf{H}W_Q, \quad \mathbf{K} = \mathbf{H}W_K, \quad \mathbf{V} = \mathbf{H}W_V, \quad W_Q, W_K, W_V \in \mathbb{R}^{D \times d_h},\tag{9}$$

where $d_h = D/n_h$ is the per-head dimension. Each head computes an independent attention output; the n_h outputs are concatenated and linearly projected back to \mathbb{R}^D . Within each head, we replace the standard softmax kernel with a positive feature map $\phi(z) = \text{elu}(z) + 1$, where $\text{elu}(z) = z$ for $z > 0$ and $e^z - 1$ for $z \leq 0$ [Clevert, Unterthiner, and Hochreiter, 2016, Katharopoulos et al., 2020]. The output for point i is

$$\text{LinAttn}(\mathbf{Q}, \mathbf{K}, \mathbf{V})_i = \frac{\phi(q_i)^\top \sum_{j=1}^N \phi(k_j) v_j^\top}{\phi(q_i)^\top \sum_{j=1}^N \phi(k_j) + \epsilon}.\tag{10}$$

The global sums $\sum_j \phi(k_j) v_j^\top$ and $\sum_j \phi(k_j)$ are computed once and reused for every query, so this path costs $\mathcal{O}(N d_h^2)$ per head rather than $\mathcal{O}(N^2 d_h)$ for standard softmax attention, and thus grows linearly with the number of mesh points.

The local path mixes nearby spatial information. On structured discretizations, the feature matrix is reshaped to a grid $\mathbf{F} \in \mathbb{R}^{N_y \times N_x \times D}$ (matching the mesh dimensions) and passed through

a depthwise-separable convolution. The depthwise part applies a separate $k \times k$ kernel to each channel,

$$[\text{DWConv}_k(\mathbf{F})]_{p,c} = \sum_{\delta \in \mathcal{K}} w_{c,\delta}^{\text{dw}} \mathbf{F}_{p+\delta,c}, \quad (11)$$

where \mathcal{K} is the kernel stencil and p indexes grid locations. A pointwise 1×1 convolution then mixes channels,

$$[\text{PWConv}(\mathbf{Z})]_{p,c'} = \sum_{c=1}^D w_{c',c}^{\text{pw}} \mathbf{Z}_{p,c}. \quad (12)$$

This factorization keeps the local path efficient while allowing each channel to learn its own spatial filter.

On unstructured node sets, the local branch uses a scaled dot-product attention restricted to a precomputed radius-neighborhood graph. Let $\mathcal{N}(i)$ denote the valid neighbor indices for point x_i , padded to at most K entries and accompanied by a binary mask $m_{ij} \in \{0, 1\}$. With separate local projections for queries, keys, and values, the local output is

$$\mathcal{L}(\mathbf{H})_i = \sum_{j \in \mathcal{N}(i)} \text{softmax}_{j \in \mathcal{N}(i)} \left(\frac{q_i^\top k_j}{\sqrt{d_h}} + \log m_{ij} \right) v_j, \quad (13)$$

where $\log m_{ij}$ equals zero for valid neighbors and is taken as $-\infty$ for padded entries ($m_{ij} = 0$), effectively excluding them from the softmax. The radius is chosen from training-set nearest-neighbor statistics. The two paths are combined as

$$\text{Attention}(\mathbf{H}) = \alpha \text{LinAttn}(\mathbf{Q}, \mathbf{K}, \mathbf{V}) + (1 - \alpha) \mathcal{L}(\mathbf{H}), \quad (14)$$

where \mathcal{L} denotes the local branch. In the reported runs, $\alpha = 0.7$ is fixed. Before the final output projection $W_{\text{out}} \in \mathbb{R}^{D \times D}$, a learned channel-wise gate $g = \sigma(W_{\text{gate}} \mathbf{H}^{\ell-1})$ modulates the combined output elementwise, allowing each feature channel to be suppressed or amplified depending on the input.

This design separates the two roles relevant to PDE surrogate modeling. The global path enables communication across the entire discretization, while the local path gives the model a learned neighborhood-dependent route for short-range spatial information. The combination is intended to match a common structure in PDE fields: local differential behavior coexists with nonlocal dependence induced by geometry, boundary conditions, or global constraints.

3.4 Decoder

After the final encoder layer, a lightweight multilayer perceptron predicts the solution at each point. The decoder uses a skip connection from the raw embedding input:

$$\hat{u}(x_i) = \text{MLP}_{\text{head}} \left(\text{RMSNORM}(h_i^L + W_{\text{skip}} s_i) \right). \quad (15)$$

This preserves the coordinate and geometry information that can be weakened by repeated global mixing.

3.5 Summary of Architectural Hyperparameters

Table 1 collects the fixed architectural hyperparameters. The model width D , depth L , and per-problem settings are listed separately in Table 2; the quantities below are shared across all experiments unless noted.

Table 1: Shared architectural hyperparameters. Here D denotes the encoder width (model dimension) and d_x is the spatial dimension of the domain Ω (Section 3). Per-problem values of D and L are given in Table 2.

Symbol / Component	Description	Value
α	Global/local attn. weight (Eq. 14)	0.7
k	Local depthwise conv. kernel	3×3
n_h	Attention heads	8
R	Ref. grid points per axis (distance enc.)	8
B	Fourier frequency bands	4
K	Max neighbors (unstruct. local attn.)	96 (Elast.); 32 (Car)
	Neighborhood radius (unstructured)	$2 \times$ median NN spacing
ϵ	RMSNorm and linear-attention constant	10^{-6}
FFN	SwiGLU hidden width	$\lfloor D \times 2/3 \rfloor$
Embedder MLP	Maps raw input s_i to width D	2 layers (Linear-GELU-Linear)
Decoder MLP	Maps final features to solution	2 layers (Linear-GELU-Linear)
Dropout	Attention and FFN	0
Weight decay	Adam regularization	10^{-5} (Car: 0)
Learning rate	Peak learning rate	10^{-3}
Schedule	Learning rate annealing	OneCycleLR (Pipe: cosine)
Epochs	Training duration	500 (Car: 200)

Table 2: Model configuration and parameter counts for the reported experiments. Reference discretizations are summarized in Table 3; the ‘‘Local mixing’’ column indicates the neighborhood representation used by LLT.

Problem	Local mixing	D	Layers	Heads	Batch	Parameters
Elasticity	radius graph	128	6	8	1	1.172M
Plasticity	convolutional	128	4	8	8	0.793M
Airfoil	convolutional	64	6	8	4	0.284M
Pipe	convolutional	64	6	8	4	0.284M
Darcy	convolutional	128	8	8	4	1.369M
Car Design	radius graph	128	8	8	1	1.458M

4 Experiments

We evaluate the model on five operator-learning benchmark problems drawn from Geo-FNO and Transolver [Li et al., 2023c], and additionally on a three-dimensional car aerodynamics dataset [Umetani and Bickel, 2018, Chang, Funkhouser, Guibas, Hanrahan, Huang, Li, Savarese, Savva, Song, Su, Xiao, Yi, and Yu, 2015]. The five benchmark problems span solid mechanics, compressible and incompressible flow, and elliptic porous-media flow. Reference solutions were generated with finite-element, finite-volume, and finite-difference solvers on structured and unstructured discretizations (Table 3). The car dataset extends the study to large unstructured three-dimensional meshes. All experiments use supervised learning from discretized input-output pairs. Test accuracy is reported as relative L_2 error for the five benchmark problems; training and test split sizes are 1000/200 for all problems except Plasticity (900/80). Problem definitions and baseline values follow the cited studies; our training settings are summarized below and in Table 2.

4.1 PDE problems

Figure 2 illustrates representative meshes for the five benchmark problems. Throughout this section, a structured discretization denotes a logically rectangular (i, j) mesh with fixed dimen-

sions $N_y \times N_x$. A structured mesh need not have uniform physical spacing; Airfoil, Pipe, and Plasticity are body-fitted structured meshes with non-uniform node spacing. Darcy is the only case with a uniform Cartesian grid. An *unstructured* discretization denotes a node set without fixed (i, j) topology, such as Elasticity and Car Design.

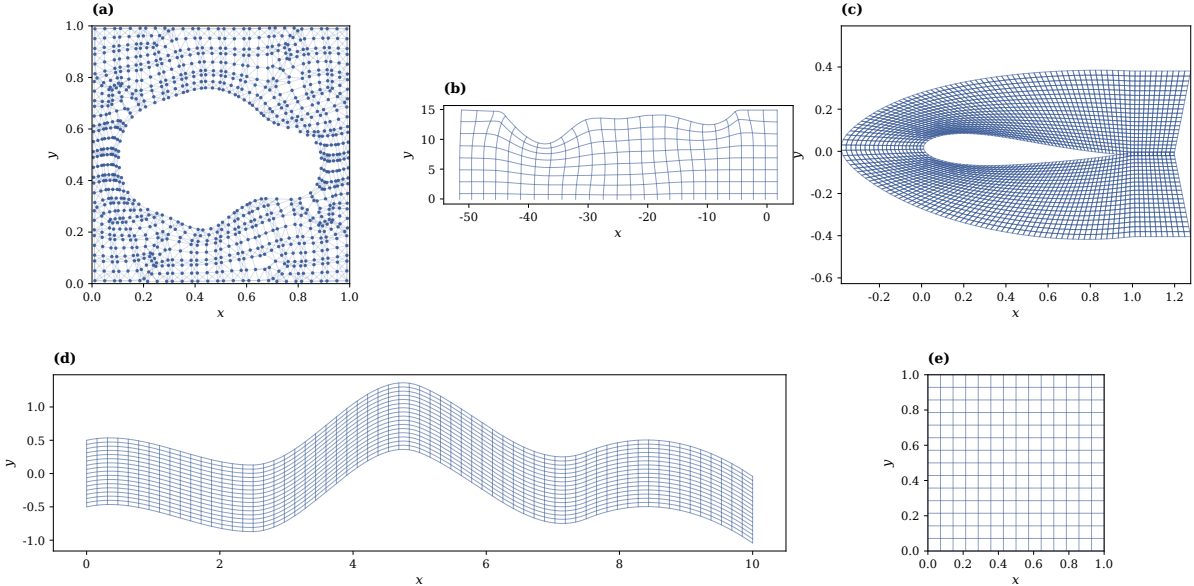


Figure 2: Representative spatial meshes for the five benchmark problems. Only discrete geometry is shown; field values are omitted. Across the top row, (a) shows the unstructured finite-element mesh with 972 nodes used in Elasticity, (b) shows the structured 101×31 Lagrangian finite-element mesh used in Plasticity, and (c) shows a cropped view of the body-fitted finite-volume C-grid used in Airfoil, whose full mesh has resolution 221×51 . The bottom row displays the structured mapped nodal grid of size 129×129 for the curved Pipe channel in (d) and the uniform 85×85 Cartesian finite-difference grid for Darcy in (e).

Table 3: Summary of the PDE problems used in the experiments. The five benchmark problems follow the Geo-FNO and Transolver conventions [Li et al., 2023c, Wu et al., 2024]; the car dataset follows the ShapeNet Car benchmark [Umetani and Bickel, 2018, Wu et al., 2024]. Structured discretizations use fixed (i, j) indexing; uniform Cartesian spacing holds only for Darcy.

Problem	Domain	Governing model	Mesh	N	Learned map
Elasticity	2D	Hyperelastic solid	Unstructured	972	Coordinates \rightarrow stress σ
Plasticity	2D+time	Elasto-plastic solid	Structured, non-uniform	3,131	Shape, time \rightarrow deformation
Airfoil	2D	Compressible Euler	Structured, non-uniform	11,271	Coordinates \rightarrow Mach number
Pipe	2D	Incompressible Navier–Stokes	Structured, non-uniform	16,641	Coordinates \rightarrow velocity u_x
Darcy	2D	Elliptic Darcy	Structured, uniform	7,225	$a(x) \rightarrow$ pressure u
Car Design	3D	Incompressible Navier–Stokes	Unstructured	32,186	Geometry \rightarrow velocity & pressure

The problems, summarized in Table 3, are selected to test different parts of the operator-learning task. Elasticity and Plasticity are solid-mechanics problems, Airfoil and Pipe are fluid problems, and Darcy is a porous-media flow problem governed by Darcy’s law [Li et al., 2021]. Elasticity tests unstructured geometry handling, Plasticity tests time conditioning and multichannel outputs, Airfoil and Pipe test flow fields on body-fitted structured meshes, and Darcy tests an elliptic coefficient-to-solution map. The datasets and reference solvers for these follow Geo-FNO [Li et al., 2023c]. Problem-specific details are given below.

Elasticity. We estimate the internal stress of an elastic material from its material structure. The solid dynamics are governed by

$$\rho^s \frac{\partial^2 \mathbf{u}}{\partial t^2} + \nabla \cdot \boldsymbol{\sigma} = 0, \quad (16)$$

where ρ^s is the material density, \mathbf{u} is displacement, and $\boldsymbol{\sigma}$ is the stress tensor. The domain is a unit cell with a randomly shaped central void; the bottom edge is clamped, and tensile traction is applied to the top edge. Reference solutions are computed with a finite-element solver using approximately 100 quadratic quadrilateral elements per sample. Each sample is stored as an unstructured node set of 972 points; the model maps node coordinates to a scalar stress value at each node. The training split contains 1000 samples with different structures, and the test split contains 200 samples.

Plasticity. We predict the deformation of a plastic material after impact from an arbitrary-shaped die. It uses the same balance law as the Elasticity case, but with an elasto-plastic constitutive model,

$$\begin{aligned} \boldsymbol{\sigma} &= \mathbf{C} : (\boldsymbol{\epsilon} - \boldsymbol{\epsilon}_p), \\ \dot{\boldsymbol{\epsilon}}_p &= \lambda \nabla_{\boldsymbol{\sigma}} f(\boldsymbol{\sigma}), \\ f(\boldsymbol{\sigma}) &= \sqrt{\frac{3}{2}} \left\| \boldsymbol{\sigma} - \frac{1}{3} \text{tr}(\boldsymbol{\sigma}) \mathbf{I} \right\|_F - \sigma_Y, \end{aligned} \quad (17)$$

with the complementarity conditions $\lambda \geq 0$, $f(\boldsymbol{\sigma}) \leq 0$, and $\lambda f(\boldsymbol{\sigma}) = 0$. Reference simulations use ABAQUS with CPS4R bilinear quadrilateral elements. The die shape is discretized on a 101×31 structured Lagrangian mesh, yielding 3131 spatial points. The target contains four displacement-related channels over 20 future time steps. We use the time-embedding setting in the model so that a single network can represent the requested output time. The training split contains 900 samples with different die shapes, and the test split contains 80 samples.

Airfoil. We estimate the Mach number around two-dimensional airfoil geometries. The flow is modeled by the inviscid compressible Euler equations,

$$\begin{aligned} \frac{\partial \rho^f}{\partial t} + \nabla \cdot (\rho^f \mathbf{v}) &= 0, \\ \frac{\partial \rho^f \mathbf{v}}{\partial t} + \nabla \cdot (\rho^f \mathbf{v} \otimes \mathbf{v} + p \mathbf{I}) &= 0, \\ \frac{\partial E}{\partial t} + \nabla \cdot ((E + p) \mathbf{v}) &= 0, \end{aligned} \quad (18)$$

where ρ^f is fluid density, \mathbf{v} is velocity, p is pressure, and E is total energy. The far-field condition uses $M_\infty = 0.8$ and an angle of attack 0, with a no-penetration condition on the airfoil. Reference solutions are generated with a second-order implicit finite-volume solver on a body-fitted C-grid. The geometries are deformations of the NACA-0012 airfoil and are discretized on a 221×51 structured mesh, giving 11271 spatial points. The model receives the coordinates of the structured mesh and predicts the scalar Mach-number field. The training split contains 1000 airfoil designs, and the test split contains 200 designs.

Pipe. We estimate the horizontal velocity field in a two-dimensional pipe flow. The governing equations are the incompressible Navier-Stokes equations,

$$\begin{aligned} \frac{\partial \mathbf{v}}{\partial t} + (\mathbf{v} \cdot \nabla) \mathbf{v} &= -\nabla p + \nu \nabla^2 \mathbf{v}, \\ \nabla \cdot \mathbf{v} &= 0, \end{aligned} \quad (19)$$

with viscosity $\nu = 0.005$. The problem imposes a parabolic inlet profile, a free outlet condition, and no slip on the pipe wall. Reference solutions are computed with an implicit Taylor-Hood finite-element solver, but the dataset stores fields on a 129×129 structured nodal grid with an analytical coordinate map (as in Geo-FNO), not the native FE connectivity. At each streamwise index, nodes lie on a vertical cross-section of nearly unit width that translates with the curved centerline; the model receives the two-dimensional coordinates of each grid point and predicts one velocity value per point. The different samples are generated by varying the pipe centerline. The training split contains 1000 samples, and the test split contains 200 samples.

Darcy. We model flow through a porous medium [Li et al., 2021, Wu et al., 2024]. The governing equation is the elliptic pressure equation

$$-\nabla \cdot (a(x)\nabla u(x)) = f(x), \quad x \in \Omega, \quad (20)$$

with a homogeneous Dirichlet boundary condition $u(x) = 0$ on $\partial\Omega$, where $\Omega = (0, 1)^2$. The input coefficient $a(x)$ represents the heterogeneous medium structure, and the output $u(x)$ is the pressure solution. Reference simulations use a finite-difference discretization on a uniform 421×421 Cartesian grid; the data are downsampled to the 85×85 grid used in the main experiments, giving 7225 spatial points. This is the only benchmark with uniform Cartesian spacing. The input features are normalized to the training distribution. The training split contains 1000 samples with different medium structures, and the test split contains 200 samples.

Car Design. We estimate the velocity and surface-pressure fields around three-dimensional car geometries [Umetani and Bickel, 2018, Wu et al., 2024]. The dataset contains 889 car shapes from the “car” category of ShapeNet [Chang et al., 2015], with reference simulations at a driving speed of 72 km/h ($\text{Re} = 5 \times 10^6$) generated by solving the incompressible Navier-Stokes equations on an unstructured three-dimensional mesh [Umetani and Bickel, 2018]. Each sample is discretized with 32,186 mesh points that cover both the surrounding air volume and the car surface. The model input combines mesh-point position, signed distance to the surface, and surface normal; the output contains three velocity components and one pressure value per point. We follow the train/test split used in prior work [Wu et al., 2024], with 789 training samples and 100 test samples.

4.2 Training protocol and hardware

The model is trained using the relative L_2 loss. Unless otherwise noted below, training uses 500 epochs, the Adam optimizer [Loshchilov and Hutter, 2019], a weight decay of 10^{-5} , and a learning rate of 10^{-3} . The batch size depends on the problem: 1 for Elasticity and Car Design, 4 for Airfoil, Pipe, and Darcy, and 8 for Plasticity. Cases with structured (i, j) indexing use the convolutional local-mixing path. Elasticity and Car Design use a radius-neighbor graph for the local branch (Table 2).

All the experiments use the same loss definition, data normalization, and evaluation procedure across the LLT runs. Checkpoints are selected based on the validation error before the test evaluation. Table 2 lists the model width, depth, batch size, and parameter count for each problem. The full list of hyperparameters is given in Table 1. All the experiments were conducted on a single NVIDIA GeForce RTX 4090 GPU.

Computational cost is measured relative to the Transolver scheme, using a common script and hardware. Each reported time is the wall-clock duration of one training iteration, defined as one forward pass followed by one adjoint (backward) pass, averaged over 30 repetitions after 10 warmup iterations. The measurements use a batch of four PDE instances. Two comparison modes are reported in Section 5.1: matched hyperparameters at prescribed grid resolutions, and the grid resolutions and model configurations from Table 2. The peak memory denotes the

maximum device memory allocated during the timed iteration. Implementation details, such as operator compilation, are held fixed across both methods in each comparison.

4.3 Evaluation

The main accuracy metric is the relative L_2 error,

$$\frac{\|\hat{u} - u\|_2}{\|u\|_2}, \quad (21)$$

computed after applying the same output normalization convention used during training. We report the error on the relevant held-out test sets of each problem.

Baseline values in the main accuracy table are taken from the cited literature unless otherwise indicated, primarily from the comparison table in Transolver [Wu et al., 2024]. Those reported baselines were the best results after the original authors’ model selection and hyperparameter searches, so we compare against the published best reported values rather than non-optimized reruns. This makes the table useful for positioning the method against established neural operator and Transformer baselines.

5 Results

Table 4 compares the relative L_2 error on the five main problems. Elasticity is the only unstructured discretization in this set; the other four use structured (i, j) -indexed meshes, three of them body-fitted and one uniform Cartesian (Table 3). Compared with the published baseline values, LLT yields the lowest reported errors for Elasticity, Plasticity, Airfoil, and Darcy. Pipe is the main exception: Transolver++ has the lowest error, while LLT remains close to the Transolver and LNO results.

The baseline values are taken from the literature, chiefly from the Transolver comparison study [Wu et al., 2024], where the listed methods are reported after their own tuning and hyperparameter searches. The table should therefore be read as a comparison against optimized published results rather than a fully controlled retraining study. Wall-clock cost is reported separately in Section 5.1 under controlled comparison conditions.

Figures 3-7 show representative predictions alongside reference solutions. In Elasticity (Figure 3), the model resolves stress concentrations around the void and along the loaded boundary on the unstructured FEM mesh, where the local branch operates through the radius-neighbor graph rather than convolution. Plasticity (Figure 4) shows the largest accuracy gain over prior methods; the multichannel displacement output at the final time step closely tracks the die-induced deformation pattern.

Darcy (Figure 5) and Airfoil (Figure 6) test different aspects of the architecture: Darcy is a scalar elliptic problem on a uniform Cartesian grid where global coupling dominates, while Airfoil requires capturing sharp gradients and near-discontinuities on a body-fitted mesh. In both cases LLT achieves the lowest error in the comparison. For Pipe (Figure 7), Transolver++ achieves a lower error; our result is comparable to Transolver and LNO. The pipe problem features smooth velocity profiles on a relatively large structured grid (129×129), so the gains from local convolution are less pronounced relative to the slice-based approach in Transolver++.

We also apply LLT to the ShapeNet Car benchmark [Umetani and Bickel, 2018, Chang et al., 2015, Wu et al., 2024], a three-dimensional external-aerodynamics problem with 32,186 unstructured mesh points per sample. Figure 8 shows predicted and reference surface pressure for three held-out car geometries. The model captures the expected pressure distribution: elevated pressure at the front stagnation region and lower pressure over the roof and side panels. The same architecture handles this 3D mesh without a convolutional local-mixing path, using the radius-neighbor graph described in Section 4.

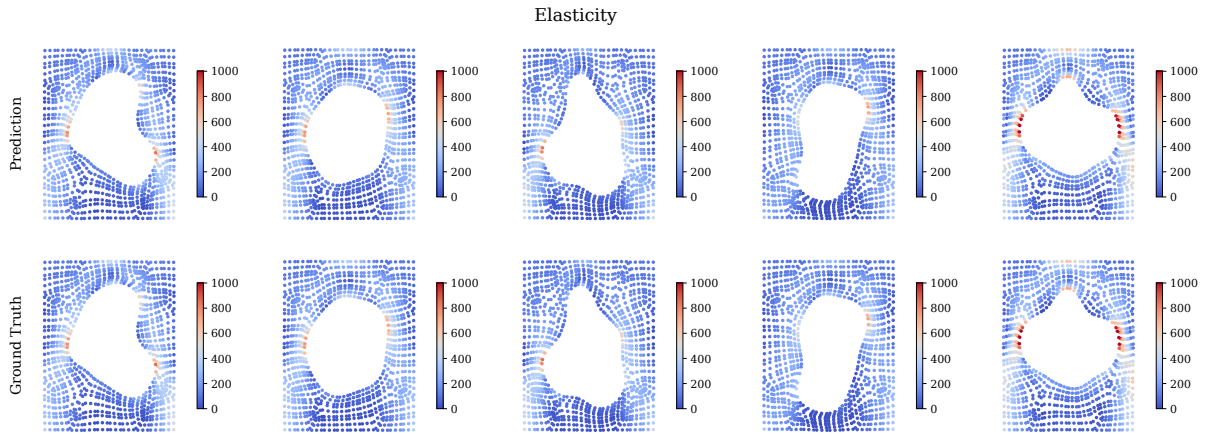


Figure 3: Elasticity: predicted stress σ (top) and reference (bottom) for five test geometries on the unstructured FEM mesh.

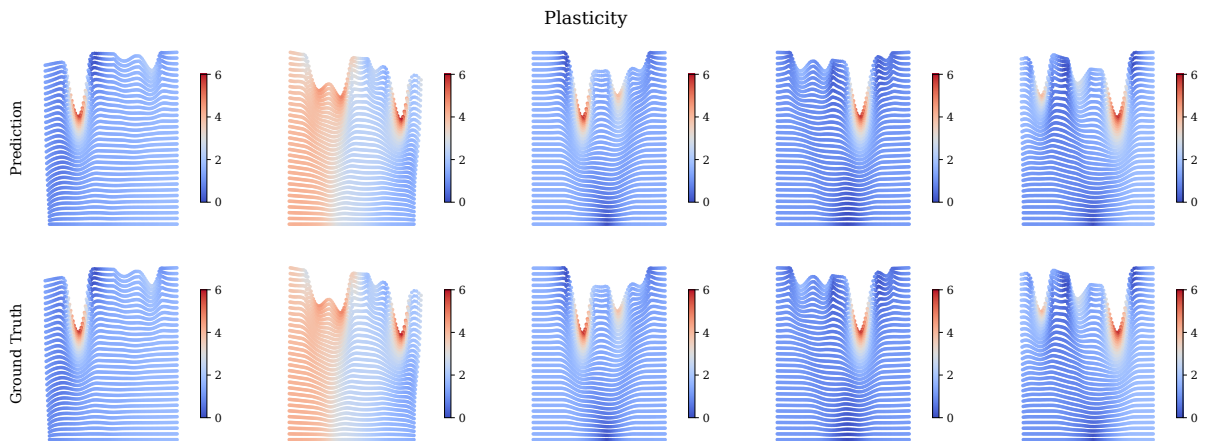


Figure 4: Plasticity: predicted displacement magnitude $\|\mathbf{u}\|$ (top) and reference (bottom) at the final time step for five test samples.

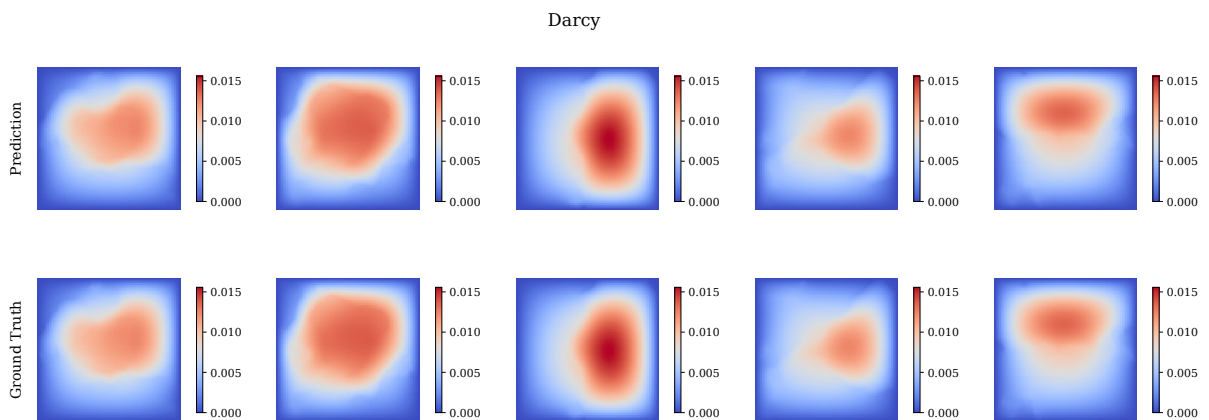


Figure 5: Darcy flow: predicted pressure u (top) and reference (bottom) for five test permeability fields.

Table 4: Relative L_2 error on the five benchmark problems (values $\times 10^{-1}$). LLT is our proposed method. **Bold** and underline denote the lowest and second-lowest error per column; “/” indicates no reported result.

Model	Relative L_2 ($\times 10^{-1}$)				
	Elasticity	Plasticity	Airfoil	Pipe	Darcy
FNO [2021]	/	/	/	/	0.1080
U-FNO [2022]	0.2390	0.0390	0.2690	0.0560	0.1830
geo-FNO [2023c]	0.2290	0.0740	0.1380	0.0670	0.1080
U-NO [2023]	0.2580	0.0340	0.0780	0.1000	0.1130
F-FNO [2023]	0.2630	0.0470	0.0780	0.0700	0.0770
LSM [2023]	0.2180	0.0250	0.0590	0.0500	0.0650
LNO [2024]	0.0690	0.0290	0.0530	<u>0.0310</u>	0.0630
Galerkin [2021]	0.2400	0.1200	0.1180	0.0980	0.0840
HT-Net [2022]	/	0.3330	0.0650	0.0590	0.0790
OFormer [2023a]	0.1830	0.0170	0.1830	0.1680	0.1240
GNOT [2023]	0.0860	0.3360	0.0760	0.0470	0.1050
FactFormer [2023b]	/	0.3120	0.0710	0.0600	0.1090
ONO [2024]	0.1180	0.0480	0.0610	0.0520	0.0760
Transolver [2024]	0.0640	0.0130	0.0530	0.0330	0.0580
Transolver++ [2025]	<u>0.0520</u>	<u>0.0110</u>	<u>0.0480</u>	0.0270	<u>0.0490</u>
LLT	0.0512	0.0058	0.0462	0.0376	0.0440

5.1 Computational cost and scaling

A central motivation for the proposed approach is computational efficiency. For a discretization with N points and per-head dimension d_h , the global linear-attention path costs $\mathcal{O}(Nd_h^2)$ per head, compared with $\mathcal{O}(N^2d_h)$ for dense softmax attention. The local path is also linear in the number of points when its spatial support is fixed: $\mathcal{O}(Nk^2D)$ for a $k \times k$ convolution on structured grids, and $\mathcal{O}(NKd_h)$ for a masked neighborhood of at most K nodes on unstructured meshes. With fixed channel width, kernel size, and neighbor count, the total encoder cost therefore grows nearly linearly with N .

We compare wall-clock cost against Transolver [Wu et al., 2024] under the protocol described in Section 4. Figure 9 and Table 5 report matched structured-grid results: both operators use identical width, depth, batch size, and discretization at each grid resolution N . The speedup

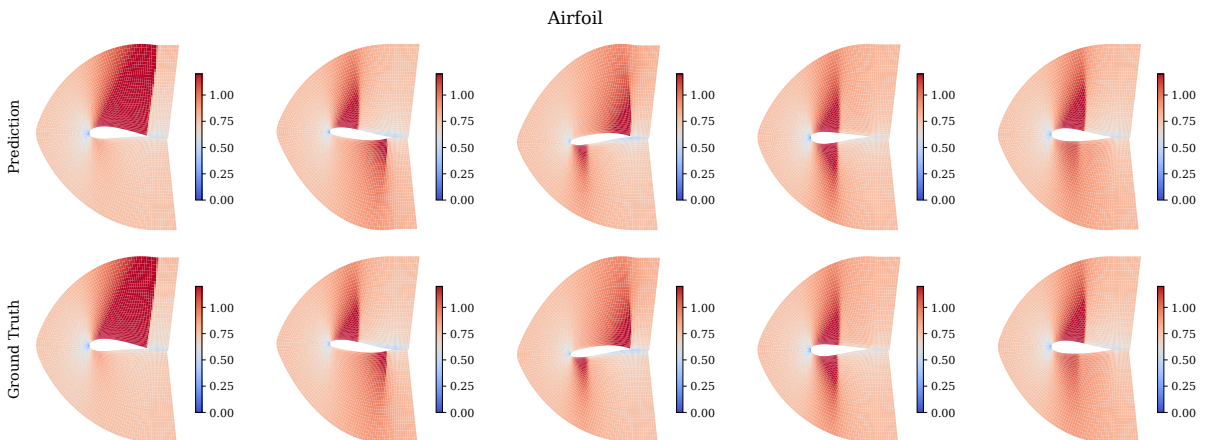


Figure 6: Airfoil flow: predicted Mach number M (top) and reference (bottom) for five test airfoil designs.

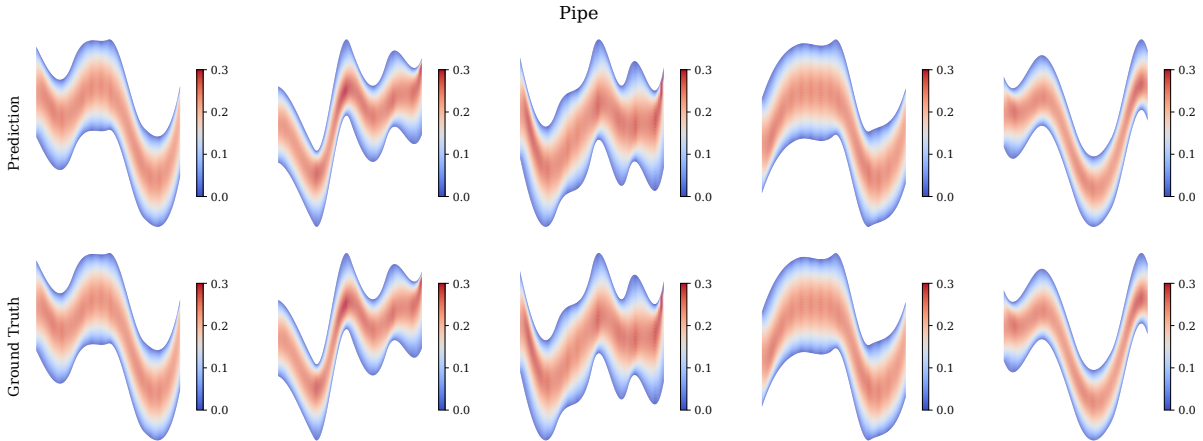


Figure 7: Pipe flow: predicted horizontal velocity u_x (top row) and reference solution (bottom row) for five test centerline geometries.

ranges from $1.78\times$ at $N = 4,096$ to $2.45\times$ at $N = 32,768$; it decreases slightly to $2.28\times$ at $N = 65,536$, likely due to memory-bandwidth saturation at that resolution. Peak memory remains comparable across the tested range.

Table 5: Matched structured-grid wall-clock cost. Speedup is Transolver time divided by LLT time; values above $1\times$ indicate a lower cost for LLT.

N	Time per iteration (ms)		Peak memory (MiB)		Speedup
	LLT	Transolver	LLT	Transolver	
4,096	9.9	17.6	694	739	1.78 \times
8,192	15.0	29.3	1384	1445	1.95 \times
16,384	31.2	71.6	2729	2855	2.29 \times
32,768	65.2	159.6	5374	5677	2.45 \times
65,536	125.5	285.6	11562	11061	2.28 \times

Figure 10 and Table 6 report the same quantities at the spatial resolutions and model configurations used for the accuracy results in Table 4. For the four structured discretizations, LLT requires less time per iteration, with speedups ranging from $2.05\times$ (Darcy) to $4.14\times$ (Pipe). The variation reflects the ratio of spatial points to model width: Pipe and Airfoil use $D = 64$ on large grids ($N > 11,000$), so the linear-attention savings in N dominate; Darcy uses $D = 128$ on a smaller grid ($N = 7,225$), where the per-head cost $\mathcal{O}(Nd_h^2)$ is a larger fraction of the total work and the relative advantage over Transolver’s slice attention is smaller. These measurements characterize the cost of one gradient-based training iteration; in deployment, data transfer, preprocessing, and forward-only inference may also contribute to the total wall-clock budget.

Table 6: Wall-clock cost at the problem-specific spatial resolutions and model configurations from Table 2; reference structured discretizations are listed in Table 3. Speedup is defined as in Table 5.

Problem	N	Time per iteration (ms)		Peak memory (MiB)		Speedup
		LLT	Transolver	LLT	Transolver	
Plasticity	3,131	9.4	27.7	592	1020	2.94 \times
Airfoil	11,271	27.9	111.0	2662	3450	3.97 \times
Pipe	16,641	42.7	176.4	3964	5734	4.14 \times
Darcy	7,225	23.1	47.3	2228	2239	2.05 \times

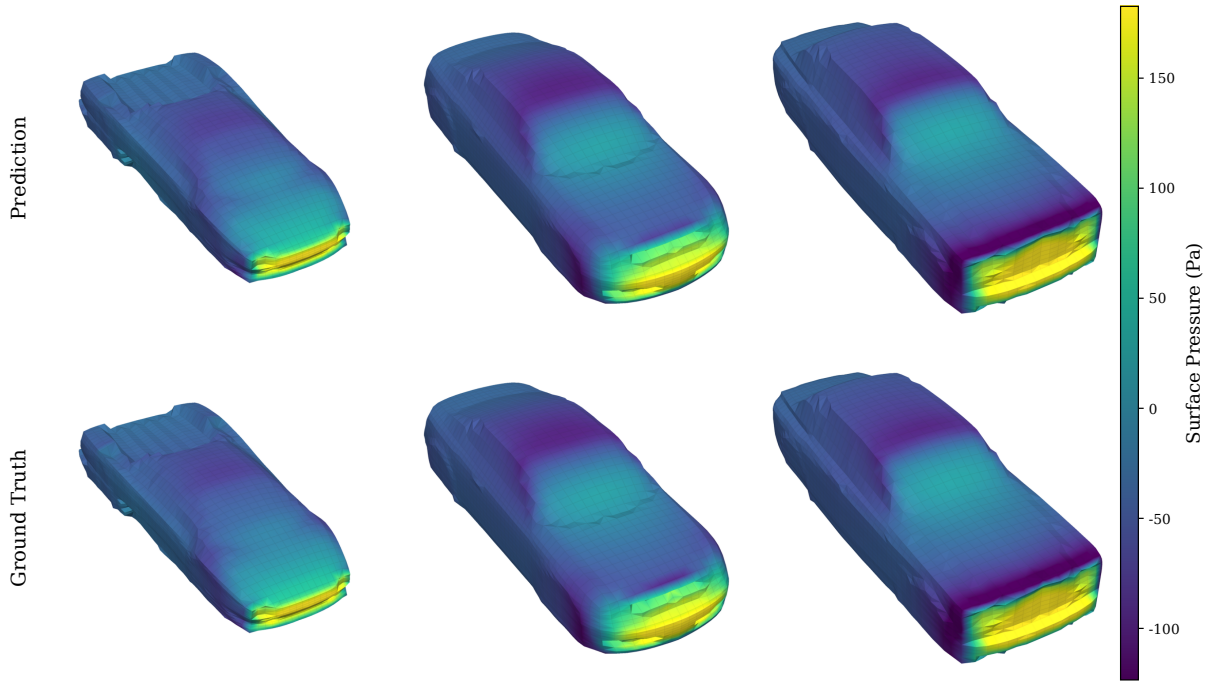


Figure 8: Car design: predicted surface pressure (top row) and reference solution (bottom row) for three test car geometries on the unstructured 3D mesh.

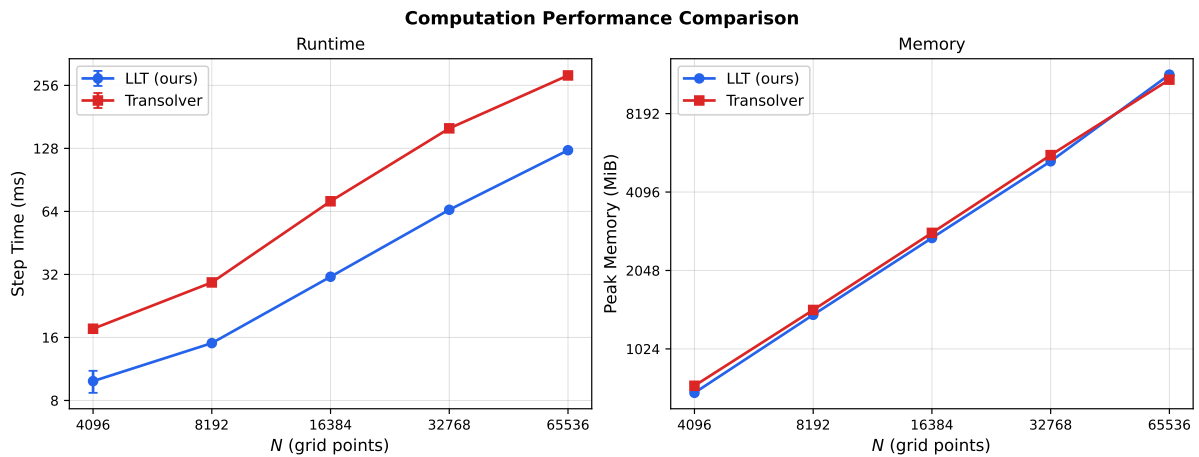


Figure 9: Computational cost versus grid resolution on structured meshes under matched settings. Left: wall-clock time per training iteration (forward and adjoint pass). Right: peak memory requirement. Both curves use identical discretizations, a batch size of four, and the measurement procedure in Section 4.

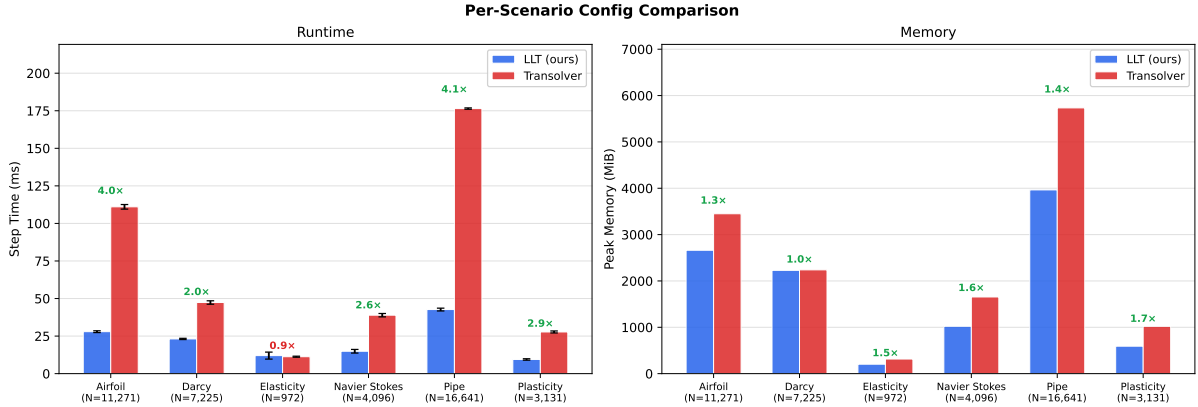


Figure 10: Computational cost at the problem-specific spatial resolutions and model configurations from Table 2. Left: wall-clock time per training iteration. Right: peak memory requirement. Speedup annotations above each pair denote Transolver time divided by LLT time.

6 Conclusion

In this study, we present Local Linear Transformer (LLT) for supervised PDE surrogate modeling. The model observes input and output fields on a finite set of mesh points and combines kernelized linear attention for domain-wide communication with an explicit local spatial-mixing path and geometry-aware encodings. The same encoder-decoder formulation applies to structured discretizations and unstructured node sets.

We evaluated LLT on five standard operator-learning benchmarks spanning elasticity, plasticity, external and internal flow, and Darcy flow, together with a three-dimensional ShapeNet Car case. On the five two-dimensional problems, LLT attains the lowest reported relative L_2 error on Elasticity, Plasticity, Airfoil, and Darcy and remains competitive on Pipe, where Transolver++ has the lowest reported error. Matched wall-clock measurements on structured meshes show lower training-step time than Transolver over the tested resolutions, with speedup increasing from $1.78\times$ at $N = 4,096$ to $2.45\times$ at $N = 32,768$. On the car dataset, the predicted surface pressure follows the reference stagnation and suction patterns across different geometries.

These results indicate that a Transformer-based operator can retain useful long-range coupling while avoiding the quadratic cost of dense attention, provided that local spatial structure is modeled explicitly. Future work may extend the same local-global design to additional three-dimensional benchmarks, physics-informed training objectives, and time-dependent problems where rollout accuracy becomes a central measure of performance.

References

- Kamyar Azizzadenesheli, Nikola Kovachki, Zongyi Li, Miguel Liu-Schiaffini, Jean Kossaifi, and Anima Anandkumar. Neural operators for accelerating scientific simulations and design. *Nature Reviews Physics*, 6(5):320–328, 2024.
- Shengze Cai, Zhiping Mao, Zhicheng Wang, Minglang Yin, and George Em Karniadakis. Physics-informed neural networks (pinns) for fluid mechanics: A review. *Acta Mechanica Sinica*, 37(12):1727–1738, 2021.
- Shuhao Cao. Choose a transformer: Fourier or galerkin. In *NeurIPS*, 2021.
- Angel X Chang, Thomas Funkhouser, Leonidas Guibas, Pat Hanrahan, Qixing Huang, Zimo Li, Silvio Savarese, Manolis Savva, Shuran Song, Hao Su, Jian Xiao, Li Yi, and Fisher Yu. ShapeNet: An information-rich 3d model repository. *arXiv preprint arXiv:1512.03012*, 2015.

- Krzysztof Choromanski, Valerii Likhoshesterov, David Dohan, Xingyou Song, Andreea Gane, Tamas Sarlos, Peter Hawkins, Jared Davis, Afroz Mohiuddin, Lukasz Kaiser, David Belanger, Lucy Colwell, and Adrian Weller. Rethinking attention with performers. In *International Conference on Learning Representations*, 2021.
- Djork-Arne Clevert, Thomas Unterthiner, and Sepp Hochreiter. Fast and accurate deep network learning by exponential linear units. In *International Conference on Learning Representations*, 2016.
- Remi Philippe Michel Dingreville, James Allen Stewart, and Elton Y Chen. Benchmark problems for the mesoscale multiphysics phase field simulator (memphis). Technical report, Sandia National Lab.(SNL-NM), Albuquerque, NM (United States), 2020.
- Robert Eymard, Thierry Gallouët, and Raphaële Herbin. Finite volume methods. *Handbook of Numerical Analysis*, 7:713–1018, 2000.
- Sergei K Godunov and I Bohachevsky. Finite difference method for numerical computation of discontinuous solutions of the equations of fluid dynamics. *Matematičeskij Sbornik*, 47(3): 271–306, 1959.
- Jayesh K Gupta and Johannes Brandstetter. Towards multi-spatiotemporal-scale generalized pde modeling. *arXiv preprint arXiv:2209.15616*, 2022.
- Zhongkai Hao, Zhengyi Wang, Hang Su, Chengyang Ying, Yinpeng Dong, Songming Liu, Ze Cheng, Jian Song, and Jun Zhu. Gnot: a general neural operator transformer for operator learning. In *Proceedings of the 40th International Conference on Machine Learning*, pages 12556–12569, 2023.
- Thomas JR Hughes. *The Finite Element Method: Linear Static and Dynamic Finite Element Analysis*. Courier Corporation, 2012.
- Angelos Katharopoulos, Apoorv Vyas, Nikolaos Pappas, and Francois Fleuret. Transformers are rnns: Fast autoregressive transformers with linear attention. In *International Conference on Machine Learning*, 2020.
- Nikola Kovachki, Zongyi Li, Burigede Liu, Kamyar Azizzadenesheli, Kaushik Bhattacharya, Andrew Stuart, and Anima Anandkumar. Neural operator: Learning maps between function spaces with applications to pdes. *Journal of Machine Learning Research*, 24(89):1–97, 2023.
- Randall J LeVeque. *Finite volume methods for hyperbolic problems*, volume 31. Cambridge university press, 2002.
- Zijie Li, Kazem Meidani, and Amir Barati Farimani. Transformer for partial differential equations’ operator learning. *TMLR*, 2023a.
- Zijie Li, Dule Shu, and Amir Barati Farimani. Scalable transformer for pde surrogate modeling. *NeurIPS*, 2023b.
- Zongyi Li, Nikola Kovachki, Kamyar Azizzadenesheli, Burigede Liu, Kaushik Bhattacharya, Andrew Stuart, and Anima Anandkumar. Neural operator: Graph kernel network for partial differential equations. *arXiv preprint arXiv:2003.03485*, 2020.
- Zongyi Li, Nikola Borislavov Kovachki, Kamyar Azizzadenesheli, Burigede liu, Kaushik Bhattacharya, Andrew Stuart, and Anima Anandkumar. Fourier neural operator for parametric partial differential equations. In *ICLR*, 2021.

- Zongyi Li, Daniel Zhengyu Huang, Burigede Liu, and Anima Anandkumar. Fourier neural operator with learned deformations for pdes on general geometries. *Journal of Machine Learning Research*, 24(388):1–26, 2023c.
- Zongyi Li, Nikola Kovachki, Chris Choy, Boyi Li, Jean Kossaifi, Shourya Otta, Mohammad Amin Nabian, Maximilian Stadler, Christian Hundt, Kamyar Azizzadenesheli, et al. Geometry-informed neural operator for large-scale 3d pdes. *Advances in Neural Information Processing Systems*, 36:35836–35854, 2023d.
- Zongyi Li, Hongkai Zheng, Nikola Kovachki, David Jin, Haoxuan Chen, Burigede Liu, Kamyar Azizzadenesheli, and Anima Anandkumar. Physics-informed neural operator for learning partial differential equations. *ACM/IMS Journal of Data Science*, 1(3):1–27, 2024.
- Xinliang Liu, Bo Xu, and Lei Zhang. HT-net: Hierarchical transformer based operator learning model for multiscale PDEs. *arXiv preprint arXiv:2210.10890*, 2022.
- Zichao Long, Yiping Lu, Xianzhong Ma, and Bin Dong. Pde-net: Learning pdes from data. In *International conference on machine learning*, pages 3208–3216. PMLR, 2018.
- Cooper Lorusso, Zijie Li, and Amir Barati Farimani. Physics informed token transformer for solving partial differential equations. *Machine Learning: Science and Technology*, 5(1):015032, 2024.
- Ilya Loshchilov and Frank Hutter. Decoupled weight decay regularization. In *International Conference on Learning Representations*, 2019.
- Lu Lu, Pengzhan Jin, Guofei Pang, Zhongqiang Zhang, and George Em Karniadakis. Learning nonlinear operators via deepoanet based on the universal approximation theorem of operators. *Nature machine intelligence*, 3(3):218–229, 2021.
- Huakun Luo, Haixu Wu, Hang Zhou, Lanxiang Xing, Yichen Di, Jianmin Wang, and Mingsheng Long. Transolver++: An accurate neural solver for pdes on million-scale geometries. In *Forty-second International Conference on Machine Learning*, 2025.
- Ben Mildenhall, Pratul P Srinivasan, Matthew Tancik, Jonathan T Barron, Ravi Ramamoorthi, and Ren Ng. Nerf: Representing scenes as neural radiance fields for view synthesis. In *European Conference on Computer Vision*, 2020.
- Vivek Oommen, Khemraj Shukla, Somdatta Goswami, Rémi Dingreville, and George Em Karniadakis. Learning two-phase microstructure evolution using neural operators and autoencoder architectures. *npj Computational Materials*, 8(1):190, 2022.
- Oded Ovadia, Adar Kahana, Eli Turkel, and Shai Dekel. Beyond the courant-friedrichs-lewy condition: Numerical methods for the wave problem using deep learning. *Journal of Computational Physics*, 442:110493, 2021.
- Oded Ovadia, Adar Kahana, Panos Stinis, Eli Turkel, Dan Givoli, and George Em Karniadakis. Vito: Vision transformer-operator. *Computer Methods in Applied Mechanics and Engineering*, 428:117109, 2024a.
- Oded Ovadia, Adar Kahana, and Eli Turkel. A convolutional dispersion relation preserving scheme for the acoustic wave equation. *Applied Mathematics and Computation*, 461:128317, 2024b.
- Oded Ovadia, Vivek Oommen, Adar Kahana, Ahmad Peyvan, Eli Turkel, and George Em Karniadakis. Real-time inference and extrapolation with time-conditioned unet: Applications in hypersonic flows, incompressible flows, and global temperature forecasting. *Computer Methods in Applied Mechanics and Engineering*, 441:117982, 2025.

- Md Ashiqur Rahman, Zachary E Ross, and Kamyar Azizzadenesheli. U-no: U-shaped neural operators. *TMLR*, 2023.
- Maziar Raissi, Paris Perdikaris, and George E Karniadakis. Physics-informed neural networks: A deep learning framework for solving forward and inverse problems involving nonlinear partial differential equations. *Journal of Computational physics*, 378:686–707, 2019.
- Pushan Sharma, Wai Tong Chung, Bassem Akoush, and Matthias Ihme. A review of physics-informed machine learning in fluid mechanics. *Energies*, 16(5):2343, 2023.
- Noam Shazeer. GLU variants improve transformer. *arXiv preprint arXiv:2002.05202*, 2020.
- Vincent Sitzmann, Julien Martel, Alexander Bergman, David Lindell, and Gordon Wetzstein. Implicit neural representations with periodic activation functions. *Advances in neural information processing systems*, 33:7462–7473, 2020.
- Maria Luisa Taccari, Oded Ovadia, He Wang, Xiaohui Chen, Adar Kahana, and Peter Jimack. Understanding the efficacy of u-net & vision transformer for groundwater numerical modelling. In *1st Workshop on the Synergy of Scientific and Machine Learning Modeling@ ICML2023*, 2023.
- Makoto Takamoto, Timothy Praditia, Raphael Leiteritz, Daniel MacKinlay, Francesco Alesiani, Dirk Pflüger, and Mathias Niepert. Pdebench: An extensive benchmark for scientific machine learning. *Advances in Neural Information Processing Systems*, 35:1596–1611, 2022.
- Matthew Tancik, Pratul P Srinivasan, Ben Mildenhall, Sara Fridovich-Keil, Nithin Raghavan, Utkarsh Singhal, Ravi Ramamoorthi, Jonathan T Barron, and Ren Ng. Fourier features let networks learn high frequency functions in low dimensional domains. In *Advances in Neural Information Processing Systems*, 2020.
- Alasdair Tran, Alexander Mathews, Lexing Xie, and Cheng Soon Ong. Factorized fourier neural operators. *arXiv preprint arXiv:2111.13802*, 2021.
- Alasdair Tran, Alexander Mathews, Lexing Xie, and Cheng Soon Ong. Factorized fourier neural operators. In *International Conference on Learning Representations*, 2023.
- Nobuyuki Umetani and Bernd Bickel. Learning three-dimensional flow for interactive aerodynamic design. *ACM Transactions on Graphics*, 37(4):89:1–89:10, 2018. doi: 10.1145/3197517.3201325.
- Ashish Vaswani, Noam Shazeer, Niki Parmar, Jakob Uszkoreit, Llion Jones, Aidan N Gomez, Lukasz Kaiser, and Illia Polosukhin. Attention is all you need. In *Advances in Neural Information Processing Systems*, 2017.
- Rui Wang, Karthik Kashinath, Mustafa Mustafa, Adrian Albert, and Rose Yu. Towards physics-informed deep learning for turbulent flow prediction. In *Proceedings of the 26th ACM SIGKDD international conference on knowledge discovery & data mining*, pages 1457–1466, 2020.
- Tian Wang and Chuang Wang. Latent neural operator for solving forward and inverse pde problems. *Advances in Neural Information Processing Systems*, 37:33085–33107, 2024.
- Gege Wen, Zongyi Li, Kamyar Azizzadenesheli, Anima Anandkumar, and Sally M Benson. U-fno—an enhanced fourier neural operator-based deep-learning model for multiphase flow. *Advances in Water Resources*, 2022.
- Haixu Wu, Jialong Wu, Jiehui Xu, Jianmin Wang, and Mingsheng Long. Flowformer: Linearizing transformers with conservation flows. *arXiv preprint arXiv:2202.06258*, 2022.

- Haixu Wu, Tengge Hu, Huakun Luo, Jianmin Wang, and Mingsheng Long. Solving high-dimensional pdes with latent spectral models. In *ICML*, 2023.
- Haixu Wu, Huakun Luo, Haowen Wang, Jianmin Wang, and Mingsheng Long. Transolver: A fast transformer solver for pdes on general geometries. In *ICML*, 2024.
- Jin-Long Wu, Heng Xiao, and Eric Paterson. Physics-informed machine learning approach for augmenting turbulence models: A comprehensive framework. *Physical Review Fluids*, 3(7): 074602, 2018.
- Zipeng Xiao, Zhongkai Hao, Bokai Lin, Zhijie Deng, and Hang Su. Improved operator learning by orthogonal attention. In *Proceedings of the 41st International Conference on Machine Learning*, 2024.
- Hao Xu, Haibin Chang, and Dongxiao Zhang. Dl-pde: Deep-learning based data-driven discovery of partial differential equations from discrete and noisy data. *arXiv preprint arXiv:1908.04463*, 2019.
- Biao Zhang and Rico Sennrich. Root mean square layer normalization. In *Advances in Neural Information Processing Systems*, 2019.
- Enrui Zhang, Adar Kahana, Eli Turkel, Rishikesh Ranade, Jay Pathak, and George Em Karniadakis. A hybrid iterative numerical transferable solver (hints) for pdes based on deep operator network and relaxation methods. *arXiv preprint arXiv:2208.13273*, 2022.
- Enrui Zhang, Adar Kahana, Alena Kopaničáková, Eli Turkel, Rishikesh Ranade, Jay Pathak, and George Em Karniadakis. Blending neural operators and relaxation methods in pde numerical solvers. *Nature Machine Intelligence*, 6(11):1303–1313, 2024.
- Chi Zhao, Feifei Zhang, Wenqiang Lou, Xi Wang, and Jianyong Yang. A comprehensive review of advances in physics-informed neural networks and their applications in complex fluid dynamics. *Physics of Fluids*, 36(10), 2024.
- Zhiyuan Zhao, Xueying Ding, and B Aditya Prakash. Pinnsformer: A transformer-based framework for physics-informed neural networks. *arXiv preprint arXiv:2307.11833*, 2023.